Journal of Materials Chemistry A

RSC Publishing

PAPER

View Article Online
View Journal | View Issue

Cite this: J. Mater. Chem. A, 2013, 1, 7905

Composite $Sr_2TiO_4/SrTiO_3$(La,Cr) heterojunction based photocatalyst for hydrogen production under visible light irradiation†

Yushuai Jia,[ab] Shuai Shen,[ab] Donge Wang,[a] Xiang Wang,[ab] Jingying Shi,[a] Fuxiang Zhang,[a] Hongxian Han*[a] and Can Li*[a]

A composite $Sr_2TiO_4/SrTiO_3$(La,Cr) heterojunction photocatalyst has been prepared by a simple *in situ* polymerized complex method. Upon Pt cocatalyst loading, this catalyst shows higher photocatalytic activity towards hydrogen production than individual $SrTiO_3$(La,Cr) and Sr_2TiO_4(La,Cr) in the presence of methanol sacrificial reagent. Microscopic morphology studies show that well defined heterojunctions are formed by matching the lattice fringes of $SrTiO_3$(La,Cr) and Sr_2TiO_4(La,Cr), and Pt was preferentially loaded on the surface of the Sr_2TiO_4(La,Cr) component in the composite $Sr_2TiO_4/SrTiO_3$(La,Cr) photocatalyst. XPS and EPR analyses show that the composite photocatalyst also has the lowest amount of Cr^{6+} electron trapping sites. Band structure analysis by combining absorption spectroscopy and Mott–Schottky plots shows that, in the composite photocatalyst, the photogenerated electrons and holes tend to migrate from $SrTiO_3$(La,Cr) to Sr_2TiO_4(La,Cr) and from Sr_2TiO_4(La,Cr) to $SrTiO_3$(La,Cr), respectively. This kind of band structure can facilitate charge transfer and separation driven by the minor potential difference between the two components, which is further confirmed by the observation of long lived electrons in the time resolved FT-IR spectroscopic study. It is concluded that the superior photocatalytic activity of the composite heterojunction photocatalyst is due to efficient charge transfer and separation by well defined heterojunctions formed between $SrTiO_3$(La,Cr) and Sr_2TiO_4(La,Cr), preferential loading of Pt nanoparticles on the Sr_2TiO_4(La,Cr) component, and the lowest amount of Cr^{6+} in the composite photocatalyst. The tailored design and synthesis of the composite heterojunction structure is a promising approach for the improvement of the photocatalytic activity of a photocatalyst.

Received 2nd April 2013
Accepted 4th May 2013

DOI: 10.1039/c3ta11326d

www.rsc.org/MaterialsA

1 Introduction

One of the most fascinating ways to produce hydrogen is photocatalytic splitting of water utilizing solar energy. So far, many materials are known to exhibit photocatalytic activity for H_2 or O_2 production half reactions in the presence of sacrificial reagent,[1] and some of the semiconductor based photocatalysts even show overall water splitting activity[2–4] although the energy conversion efficiencies are still low. In order to efficiently split water, a photocatalyst should be visible light responsive, and assembled in such a way that it can efficiently promote charge separation and migration by inhibiting undesired charge recombination.[5–7] Among the vast majority of the active photocatalysts for water splitting, layer structured perovskite titanates are considered as one of the ideal building blocks for the assembly of a water splitting photocatalyst.[8] Perovskite titanates are n-type semiconductors constituted of earth abundant elements, and usually are stable in aqueous solutions. However, the large bandgaps of the titanates (>3.0 eV) correspond to the ultraviolet (UV) light region, which shares only around 3–5% of the solar radiation spectrum. Doping of foreign elements into UV-active metal oxides is an effective method being employed for the extension of the light absorption of a semiconductor into the visible region.[9–11] It was found that Cr doping is an effective way to shift the light absorption of the titanates into the visible region for hydrogen production from aqueous methanol solutions.[12,13] However, doping also creates defect sites acting as charge recombination centers. To solve this problem, codoping methodologies are applied. It was reported recently that codoping of $SrTiO_3$ with Cr^{3+}/Sb^{5+},[14] Cr^{3+}/Ta^{5+},[15] Cr^{3+}/La^{3+} [16] can reduce the amount of charge recombination centers by keeping the charge balance and suppressing the formation of undesired Cr^{6+} electron trapping sites.

[a]State Key Laboratory of Catalysis, Dalian Institute of Chemical Physics, Chinese Academy of Sciences, Dalian National Laboratory for Clean Energy, Dalian, 116023, China. E-mail: canli@dicp.ac.cn; hxhan@dicp.ac.cn; Fax: +86-411-84694447; Tel: +86-411-84379760

[b]Graduate University of Chinese Academy of Sciences, Beijing, 100049, China

† Electronic supplementary information (ESI) available: Optimization of the photocatalyst performance, the ratio of Sr_2TiO_4(La,Cr) to $SrTiO_3$(La,Cr) in the $Sr_2TiO_4/SrTiO_3$(La,Cr) composite photocatalyst and SEM images of 1.0 wt% Pt loaded $Sr_2TiO_4/SrTiO_3$(La,Cr) sample. See DOI: 10.1039/c3ta11326d

Assembly of a multi-component composite photocatalyst might be an ideal approach to achieve efficient charge separation for enhancing photocatalytic activity of water splitting, since no great achievement has been made so far on single component photocatalysts, such as TiO_2. Lee's group[17,18] reported that formation of a p-n junction between n-type and p-type semiconductors can efficiently separate photogenerated charges and enhance the photocatalytic activity. Ye *et al.*[19] reported that a Cr-doped $Ba_2In_2O_5/In_2O_3$ composite photocatalyst system can drive both water oxidation and reduction half reactions under visible light irradiation. In this kind of composite photocatalyst approach, proper design and fabrication of the interface between the different components should be essential and necessary. We found that formation of surface phase junction of anatase/rutile,[20] heterojunction of MoS_2/CdS,[21,22] and solid solution junction of $ZnO/Zn_{2-x}GeO_{4-x-3y}N_{2y}$[23] have positive effects on the improvement of the photocatalytic activities either in hydrogen production or water oxidation half reactions. In order to facilitate charge transfer and separation in the composite photocatalyst, at least two crucial factors must be carefully considered, *i.e.*, redox (band structure) matching and lattice structure matching of the junctioned/interfaced components.

In this work, we have prepared a composite $Sr_2TiO_4/SrTiO_3$(La,Cr) heterojunction photocatalyst by a simple *in situ* polymerized complex method. In photocatalytic H_2 production reaction under visible light irradiation in the presence of methanol sacrificial reagent, this composite heterojunction based photocatalyst shows much higher photocatalytic activity than the individual $SrTiO_3$(La,Cr) and Sr_2TiO_4(La,Cr). It was found that formation of well defined heterojunctions between $SrTiO_3$(La,Cr) and Sr_2TiO_4(La,Cr), preferential loading of Pt as cocatalyst on the surface of the Sr_2TiO_4(La,Cr) component, and the lowest amount of Cr^{6+} formation in the composite heterojunction $Sr_2TiO_4/SrTiO_3$(La,Cr) photocatalyst are accountable for the efficient charge transfer and separation, hence enhancing the photocatalytic activity.

2 Experimental section

2.1 Synthesis of materials

$SrTiO_3$(La,Cr), Sr_2TiO_4(La,Cr) and $Sr_2TiO_4/SrTiO_3$(La,Cr) were prepared by the polymerized complex method.[24,25] In a typical procedure for the synthesis of $SrTiO_3$(La,Cr) and Sr_2TiO_4(La,Cr), 4.0507 g titanium tetra-isopropoxide (J&K Chemical; 98+%) was dissolved in 33.5 mL ethylene glycol (Sinopharm Chemical; ≥99.0%), followed by addition of 31.521 g citric acid (Kermel Chemical; ≥99.5%). The reaction mixture was vigorously stirred at 50 °C until it became transparent. 3.0157 g and 6.1505 g $Sr(NO_3)_2$ (Guangfu Chemical; 99.5%) were added to the reaction mixture for the synthesis of $SrTiO_3$(La,Cr) and Sr_2TiO_4(La,Cr), respectively. After the addition of $Sr(NO_3)_2$, 0.3248 g $La(NO_3)_3\cdot 6H_2O$ (Kermel Chemical; ≥98.5%) and 0.3001 g $Cr(NO_3)_3\cdot 9H_2O$ (J&K Chemical; 99%) were also added and further stirred at 50 °C for 4 h to yield a completely dissolved reaction mixture. The solution was polyesterified at 130 °C for 20 h, followed by pyrolysis at 350 °C for 2 h. The resulting black solid product was then ground into a powder and calcined on an Al_2O_3 plate at 900 °C for 2 h in air in a temperature programmed Muffle furnace. The calcined samples were kept in vials and stored in a desiccator. For the preparation of $Sr_2TiO_4/SrTiO_3$(La,Cr), 2.7005 g titanium tetra-isopropoxide was dissolved in 22.3 mL ethylene glycol, followed by addition of 21.014 g citric acid. 3.0686 g $Sr(NO_3)_2$, 0.2001 g $Cr(NO_3)_3\cdot 9H_2O$ and different amounts of $La(NO_3)_3\cdot 6H_2O$ (the molar ratios of [La]/[Cr] were 0.75, 1.00 and 1.25) were added to the reaction mixture. Other procedures were the same as the those of $SrTiO_3$(La,Cr) and Sr_2TiO_4(La,Cr).

Pt cocatalyst was loaded on the synthesized photocatalysts with H_2PtCl_6 as Pt precursor, applying the standard impregnation method.[26] In the $Pt^{4+} \rightarrow Pt$ reduction process, formation of Cr^{6+} at high temperature should be avoided since it acts as an electron trapping site. For optimization of the Pt reduction temperature in our experiments, reduction of Pt^{4+} to Pt was carried out in H_2 flow at elevated temperatures.

2.2 Characterizations of materials

The crystallinity of the synthesized samples was studied by X-ray Diffraction (XRD) technique on a Rigaku D/Max-2500/PC powder diffractometer. The measurement was performed using CuK_α as the radiation source with operating voltage of 40 kV and current of 200 mA. The scanning rate was kept at 5° min^{-1} with a step size of 0.02° in the 2θ range of 10–80°. UV-Vis Diffuse Reflectance spectra (DRS) were recorded on a UV-Vis spectrophotometer (JASCO V-550) equipped with an integrating $BaSO_4$ sphere. The morphology of the samples was examined by Scanning Electron Microscopy (SEM) images taken with a Quanta 200FEG scanning electron microscope. TEM and HRTEM images were obtained on Tecnai G^2 F30 S-Twin (FEI company) microscope with an acceleration voltage of 300 kV. The amounts of the Pt loading are 0.155, 0.163 and 0.164 wt% for $SrTiO_3$(La,Cr), Sr_2TiO_4(La,Cr) and $Sr_2TiO_4/SrTiO_3$(La,Cr) composite samples, respectively, determined by Inductively Coupled Plasma Mass Spectrometry (ICP-MS) on an ICPS-8100. The BET surface areas of the samples were calculated based on the nitrogen adsorption isotherms at 77 K performed on a Micromeritics ASAP 2000 adsorption analyzer. X-ray Photoelectron Spectroscopy (XPS) were recorded on a Thermo Escalab 250 equipped with a monochromatic AlK_α X-ray source. Electron Paramagnetic Resonance (EPR) spectra were recorded at 77 K on a Bruker ESR A200 spectrometer. The settings for the EPR measurement parameters were as follows: center field, 3360.000 G; sweep width, 6000.000 G; microwave frequency, ~9.389 GHz; modulation frequency, 100 kHz; power, 0.792 mW. The time-resolved (ms) Fourier Transform Infrared (FT-IR) spectroscopy was recorded on a Nicolet 870 FT-IR spectrometer equipped with a MCT (Mercury cadmium telluride, HgCdTe) detector and 355 nm laser pulse of 6–8 ns duration. The decay curves were recorded at room temperature by accumulating 50 traces repeated at 1 Hz.

2.3 Photocatalytic reactions

The photocatalytic H_2 production reactions were carried out in a Pyrex reaction cell connected to a closed gas circulation and evacuation system. Photocatalyst (0.5 g) was suspended in 200 mL aqueous solution containing 40 mL methanol and

thoroughly degassed by evacuation. The photocatalytic reaction was performed by photoirradiation of the reaction mixture using a 300 W Xe lamp (Ushio-CERMAX LX300) equipped with an optical cutoff filter (Kenko, L-42; $\lambda > 420$ nm) and a water filter to prevent passing of the ultraviolet and infrared light, respectively. The temperature of the reaction mixture was maintained at 288 ± 1 K by a continuous flow of cooling water. The amounts of the evolved H_2 were determined by on line gas chromatography (Shimadazu; GC-8A, MS-5A column, TCD, Ar Carrier). The amounts of produced H_2 at 5 h reaction time were used for evaluating the photocatalytic activities of the samples.

2.4 Photoelectrochemical measurements

The flat-band potentials of $SrTiO_3$(La,Cr) and Sr_2TiO_4(La,Cr) were determined by extrapolation of the Mott–Schottky plots measured on a standard three-electrode cell electrochemical workstation (CHI660A, Shanghai Chenhua Instruments, China). In this system, a Pt plate was used as counter electrode, a saturated calomel electrode (SCE) was employed as reference electrode, and the thin films of the photocatalyst samples fabricated by electrophoretic deposition method were used as the working electrode. The electrolyte was 0.5 M Na_2SO_4 solution.

Photocurrent measurements were carried out by suspension of the photocatalyst (25 mg) in distilled H_2O (75 mL) containing acetate (0.1 M) and Fe^{3+} (0.1 mM) as electron donor and acceptor, respectively.[18,27] The pH value of the suspension was adjusted to 1.8 with $HClO_4$. A Pt plate (2 × 2 cm^2, both sides were exposed to the solution), a saturated calomel electrode (SCE), and a Pt gauze were used as working (collector), reference, and counter electrodes, respectively. About +0.6 V *vs.* SCE bias potential was applied on the Pt electrode. All the experiments were conducted under the same experimental conditions with continuous purging of Ar gas into the suspension.

3 Results and discussion

3.1 Photocatalytic reactions

$SrTiO_3$(La,Cr), Sr_2TiO_4(La,Cr) and $Sr_2TiO_4/SrTiO_3$(La,Cr) composite samples with the same amounts of codoped La and Cr and Pt loadings were synthesized under the same experimental conditions. The photocatalytic activities of these samples toward H_2 production at 5 h reaction time in the presence of CH_3OH as electron donating sacrificial reagent are shown in Fig. 1. It can be seen that the photocatalytic activities of $SrTiO_3$(La,Cr) and Sr_2TiO_4(La,Cr) are relatively low, but the composite $Sr_2TiO_4/SrTiO_3$(La,Cr) photocatalyst shows a photocatalytic activity up to 6.4 and 3.0 times of the individual $SrTiO_3$(La,Cr) and Sr_2TiO_4-(La,Cr), respectively. An induction period at the initial stage of the photocatalytic reactions was also observed in the time course study (inset of Fig. 1).[15] The photocatalyst was further optimized for the Pt reduction temperature and the amount of Pt cocatalyst loading. It was found that the optimized Pt reduction temperature is between 573 K and 623 K (Fig. S1a†). In the following reactions, the temperature of 623 K was used as the fixed Pt reduction temperature. Examination of the amount of Pt loading

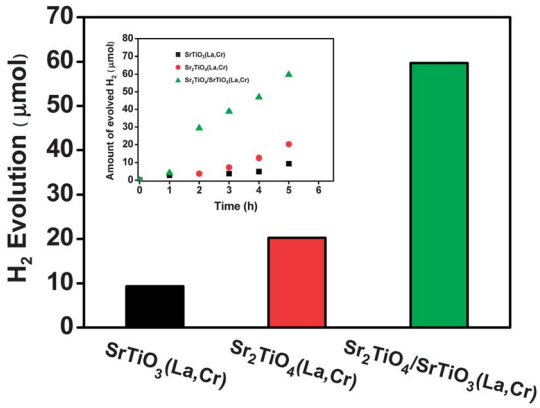

Fig. 1 Photocatalytic H_2 production activities of the initially synthesized $SrTiO_3$(La,Cr), Sr_2TiO_4(La,Cr) and $Sr_2TiO_4/SrTiO_3$(La,Cr) composite samples ([Cr]/([Ti] + [Cr]) = 0.05, [La]/[Cr] = 1.00, molar ratio). Inset: the time course of H_2 evolution.

at the reduction temperature of 623 K shows that the optimized Pt loading is 0.25 wt% (Fig. S1b†). In summary, the composition of the optimized composite photocatalyst under our experimental conditions is as follows: $Sr_2TiO_4/SrTiO_3$(La,Cr) with [La] : [Cr] : ([Ti] + [Cr]) = 5 : 4 : 80, 0.25 wt% Pt loading, and reduction of Pt in hydrogen flow at 623 K. Corresponding individual $SrTiO_3$(La,Cr) and Sr_2TiO_4(La,Cr) samples used for comparison in the following sections were also prepared under the same optimized experimental conditions.

3.2 Crystalline structures and morphologies

XRD patterns of the prepared samples are shown in Fig. 2. The $SrTiO_3$ (Fig. 2a) sample shows the characteristic diffraction peaks of (110), (111), (200) and (211) at 2θ of 32.57°, 40.14°, 46.64° and 57.94°, respectively, indicating that the synthesized $SrTiO_3$ is of cubic structure (JCPDS-84-0443). After La and Cr doping, these peaks are well preserved and no additional

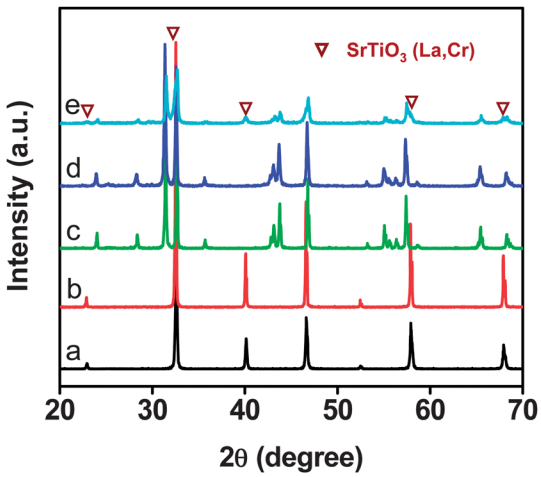

Fig. 2 X-ray diffraction patterns of the as-prepared samples: (a) $SrTiO_3$, (b) $SrTiO_3$(La,Cr), (c) Sr_2TiO_4, (d) Sr_2TiO_4(La,Cr), and (e) $Sr_2TiO_4/SrTiO_3$(La,Cr).

impurity peaks are observed (Fig. 2b), showing that doping of La and Cr did not alter the cubic structure of $SrTiO_3$. A similar doping effect was also observed when La and Cr were doped into the tetragonal structured Sr_2TiO_4 (JCPDS-39-1471). Comparison of the XRD patterns of Sr_2TiO_4 (Fig. 2c) and Sr_2TiO_4(La,Cr) (Fig. 2d) shows that all of the domain diffraction peaks of the Sr_2TiO_4 were well maintained in the La and Cr codoped Sr_2TiO_4(La,Cr) sample. Fig. 2e shows the XRD pattern of the La and Cr codoped $Sr_2TiO_4/SrTiO_3$ composite photocatalyst. Both $SrTiO_3$ and Sr_2TiO_4 diffraction peaks indicate that the cubic structured $SrTiO_3$ and tetragonal structured Sr_2TiO_4 crystallite phases are all well maintained in the composite photocatalyst. It was reported that, in La and Cr codoped titanate,[16,28] La^{3+} usually replaces the Sr sites and Cr^{3+} replaces the Ti sites. Thus the crystalline structure of the original titanate can be well preserved, and the formation of Cr^{6+} can be largely suppressed due to charge balancing between the doped cations. The ratio of Sr_2TiO_4(La,Cr) to $SrTiO_3$(La,Cr) in the $Sr_2TiO_4/SrTiO_3$(La,Cr) composite photocatalyst was determined to be approximately 3 : 2 by Le Bail whole-pattern analysis from XRD data (Fig. S2†).

SEM images (Fig. 3) in 50 nm scale show that these three samples are quite different in surface morphology. The $SrTiO_3$-(La,Cr) sample has a smooth surface with the size varying from tens to hundreds of nanometers (Fig. 3a), while the Sr_2TiO_4-(La,Cr) sample has a relatively rough surface made up of irregularly shaped aggregates with size *ca.* 5–10 nm (Fig. 3b). Interestingly, the $Sr_2TiO_4/SrTiO_3$(La,Cr) sample is composed of two big nanoparticles with distinctly different surface morphologies, one is smooth and the other one is rough (Fig. 3c). Based on the morphological features, these two nanoparticles can be assigned to $SrTiO_3$(La,Cr) and Sr_2TiO_4(La,Cr), respectively. Observation of the close contact of individual $SrTiO_3$(La,Cr) and Sr_2TiO_4(La,Cr) in the composite photocatalyst is consistent with the XRD results. In other words, the composite photocatalyst possesses a kind of superlattice macrostructure integrated with $SrTiO_3$(La,Cr) and Sr_2TiO_4(La,Cr) nanoparticles throughout the sample. Because Pt was loaded in less than 0.2 wt% per ICP-MS analysis results and the formed Pt nanoparticles are highly dispersed on the samples, we encountered some difficulties in finding the Pt sites in SEM images. However, sparsely dispersed Pt nanoparticles with size smaller than 5 nm can be visualized as white spots with relatively sharp contrast shown in the arrow directed areas in each of the images of the samples (Fig. 3a–c). It was also noted that Pt was preferentially loaded on the rough surface of the Sr_2TiO_4(La,Cr) component instead of the relatively smooth surface of the $SrTiO_3$(La,Cr) component of the $Sr_2TiO_4/SrTiO_3$(La,Cr) composite photocatalyst. We deliberately prepared $Sr_2TiO_4/SrTiO_3$(La,Cr) with 1.0 wt% Pt loading. As shown in Fig. S3,† the overall tendency of the Pt deposition is similar to the sample with 0.2 wt% Pt loading. But due to higher Pt loadings, small amounts of Pt are also occasionally deposited on the smooth surface of the $SrTiO_3$(La,Cr). This further confirms that Pt nanoparticles are preferentially loaded on the rough surface of Sr_2TiO_4(La,Cr). Preferential loading of Pt on Sr_2TiO_4(La,Cr) might be due to a better interfacial interaction (sticking) of Pt to the rough surface substrate of Sr_2TiO_4(La,Cr).

Fig. 4 shows the TEM (Fig. 4a) and HRTEM images (Fig. 4b) of the $Sr_2TiO_4/SrTiO_3$(La,Cr) composite photocatalyst. The dark contrast in the TEM image is due to thickness difference in that particular area. The HRTEM image clearly shows the existence of individual Sr_2TiO_4(La,Cr) and $SrTiO_3$(La,Cr) crystalline particles in the $Sr_2TiO_4/SrTiO_3$(La,Cr) composite photocatalyst, as identified by the corresponding (103) and (111) lattice fringe parameters of 2.84 Å and 2.24 Å, respectively. These lattice fringe parameters match well with the corresponding lattice parameters calculated by XRD. The HRTEM image also shows that a well defined heterojunction between Sr_2TiO_4(La,Cr) and $SrTiO_3$(La,Cr) nanoparticles is formed by merging the lattice fringes of the respective (103) and (111). Formation of such a kind of well matched heterojunction is expected to facilitate charge transfer and separation between the nanoparticles, thereby enhancing the photocatalytic activity.[21–23]

3.3 Band structures and charge carrier properties

Fig. 5a shows the DRS spectra of the samples. The undoped $SrTiO_3$ and Sr_2TiO_4 are only UV responsive with absorption edges at *ca.* 380 nm. However, upon La and Cr codoping, the absorption edges of these samples are extended to the visible region. At the same doping level, the absorption edges of the $SrTiO_3$(La,Cr), Sr_2TiO_4(La,Cr) and composite $Sr_2TiO_4/SrTiO_3$(La,Cr) samples lie

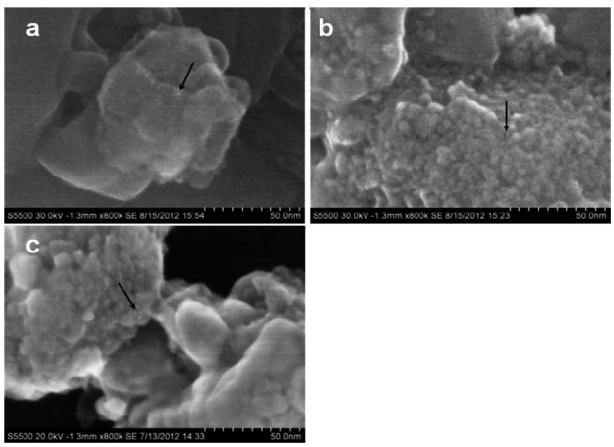

Fig. 3 SEM of Pt loaded (a) $SrTiO_3$(La,Cr), (b) Sr_2TiO_4(La,Cr), and (c) $Sr_2TiO_4/SrTiO_3$(La,Cr).

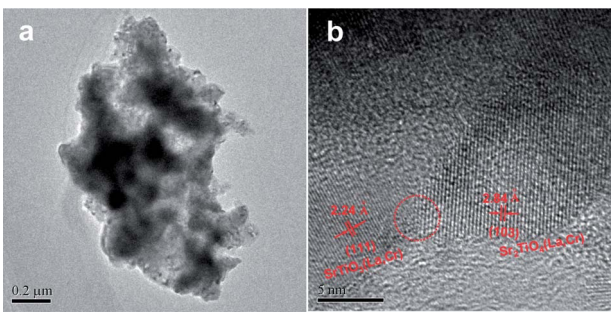

Fig. 4 (a) TEM and (b) HRTEM of the $Sr_2TiO_4/SrTiO_3$(La,Cr) composite sample.

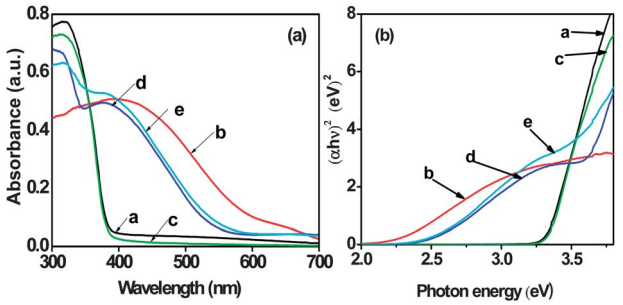

Fig. 5 (a) UV-Vis diffuse reflectance spectra and (b) plots of the $(\alpha h\nu)^2$ *vs.* photon energy ($h\nu$) of the as-prepared samples: (a) $SrTiO_3$, (b) $SrTiO_3$(La,Cr), (c) Sr_2TiO_4, (d) Sr_2TiO_4(La,Cr) and (e) $Sr_2TiO_4/SrTiO_3$(La,Cr).

at *ca.* 650 nm, 570 nm and 580 nm, respectively. The similar absorption edge of the composite $Sr_2TiO_4/SrTiO_3$(La,Cr) sample (580 nm) to that of Sr_2TiO_4(La,Cr) (570 nm) is an indication that Cr is more preferentially doped into the more open structured Sr_2TiO_4 lattice rather than $SrTiO_3$ (650 nm).[29] The visible light absorption upon La and Cr codoping is mainly due to bandgap narrowing by Cr^{3+} dopant whose occupied 3d orbital overlaps with the O 2p valance band of the strontium titanate.[12]

The bandgap energies of the La and Cr codoped samples were determined by extrapolation of the plots of the $(\alpha h\nu)^2$ *vs.* photon energy ($h\nu$) (Fig. 5b) and calculated by the following formula:[30] $\alpha h\nu = A(h\nu - E_g)^{n/2}$, where α, ν, E_g, and A are the absorption coefficient, light frequency, bandgap, and a constant value, respectively. The index n depends on the characteristics of the transition in a semiconductor, *i.e.*, direct transition ($n = 1$) or indirect transition ($n = 4$). The best fit of $(\alpha h\nu)^2$ *versus* E_g was obtained only when n is 1, suggesting that direct transitions across the energy bandgaps of these materials are allowed. So the bandgap energies of the synthesized materials (Table 1) were estimated by the interception of the tangent to the *x*-axis. The bandgaps of Sr_2TiO_4 and $SrTiO_3$ are evaluated to be 3.34 eV and 3.32 eV, respectively. While the bandgaps of La and Cr codoped Sr_2TiO_4 and $SrTiO_3$ are 2.54 eV and 2.26 eV, respectively. As for the $Sr_2TiO_4/SrTiO_3$(La,Cr) composite material, the observed bandgap is 2.52 eV, the value of which is more close to that of the Sr_2TiO_4(La,Cr).

Both Sr_2TiO_4(La,Cr) and $SrTiO_3$(La,Cr) are n-type semiconductors as shown in Fig. 6a. Upon photoexcitation of an n-type semiconductor, the photoexcited electrons and holes tend to migrate to the interior bulk and surface, respectively. However, the photoexcited electrons can migrate further to the metal cocatalyst (such as Pt) if a metal with appropriate Fermi level is loaded on the surface.[31] To address the charge transfer properties of the composite photocatalyst, we estimated the relative band structures of individual Sr_2TiO_4(La,Cr) and $SrTiO_3$(La,Cr). Fig. 6a shows the Mott–Schottky curves measured in 0.5 M Na_2SO_4 solution. The flat-band potentials of Sr_2TiO_4(La,Cr) and $SrTiO_3$(La,Cr) were obtained by the extrapolation of the Mott–Schottky plots (C^{-2} *vs.* E, electrode potential) using the following equation: $C_{sc}^{-2} = 2(E - E_{fb} - \kappa T/e)/e\varepsilon\varepsilon_0 N_D$.[32] It can be seen that the E_{fb} of Sr_2TiO_4(La,Cr) is about −1.36 V, which is more positive than that of $SrTiO_3$(La,Cr) by *ca.* 0.1 V. This value is in good agreement with the data reported in the literature.[33] By further considering that the bandgaps of Sr_2TiO_4(La,Cr) and $SrTiO_3$(La,Cr) are 2.54 eV and 2.26 eV, the valence band of Sr_2TiO_4(La,Cr) can be estimated to be roughly *ca.* 0.38 eV more positive than that of $SrTiO_3$(La,Cr). Based on these calculation results, the band structure of the composite photocatalyst can be depicted as shown in Scheme 1. Thermodynamically, under visible light irradiation, the photoexcited electrons and holes are more readily transferred from $SrTiO_3$(La,Cr) to Sr_2TiO_4(La,Cr) and from Sr_2TiO_4(La,Cr) to $SrTiO_3$(La,Cr), respectively.

Charge transfer properties of the composite photocatalyst under visible light irradiation were further evaluated by measuring the photocurrent time courses of the samples suspended in an aqueous solution containing acetate and Fe^{3+} as electron donor and acceptor, respectively (Fig. 6b). It was found that $Sr_2TiO_4/SrTiO_3$(La,Cr) composite photocatalyst generates a much higher photocurrent under visible light irradiation than the individual Sr_2TiO_4(La,Cr) or $SrTiO_3$(La,Cr). A high photocurrent implies that the composite $Sr_2TiO_4/SrTiO_3$(La,Cr) heterojunction photocatalyst generates more charges on the surface to be delivered to the electrode *via* the electrolyte. In other words, upon photoexcitation, the composite photocatalyst can have more photogenerated charges available on the surface to participate in the surface reactions, hence enhancing the photocatalytic activity.

In Cr-doped titanate semiconductor photocatalysts, formation of Cr^{6+} should be avoided since the Cr^{6+} 3d orbital level is usually located below the Ti 3d conduction band level and acts as an electron trapping site.[12,14,15,34] XPS and EPR spectroscopy

Table 1 Bandgaps (E), absorption edges (λ_{ab}) and BET surface areas of the samples. λ_{ab} was derived from $\lambda_{ab} = 1240/E$,[39] where E is the bandgap of the photocatalysts

	Bandgap energy		
Photocatalyst	E/eV	λ_{ab}/nm	BET surface area/m^2 g^{-1}
$SrTiO_3$	3.32	373	5.8
Sr_2TiO_4	3.34	371	3.7
$SrTiO_3$(La,Cr)	2.26	549	8.9
Sr_2TiO_4(La,Cr)	2.54	488	6.1
$Sr_2TiO_4/SrTiO_3$(La,Cr)	2.52	492	6.2

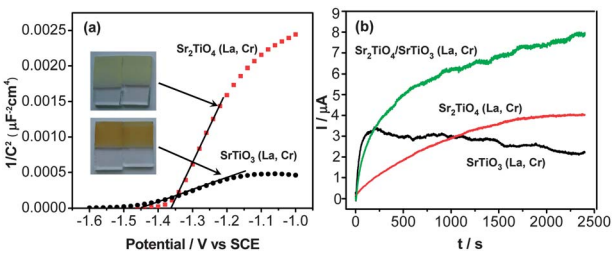

Fig. 6 (a) Mott–Schottky plots of the samples, and (b) photocurrent time courses of the samples under visible light irradiation. During the measurements, the samples were suspended in aqueous solution containing sodium acetate and iron sulfate.

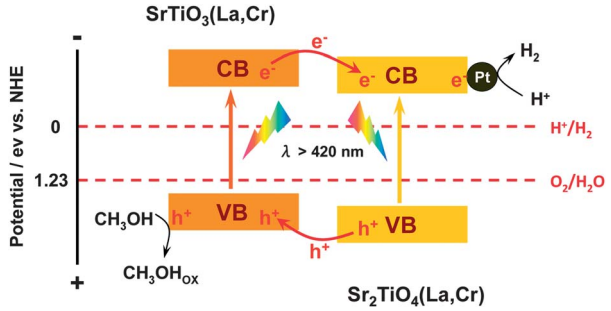

Scheme 1 Schematic band structure of La and Cr codoped $Sr_2TiO_4/SrTiO_3$ and its mechanism for H_2 production under visible light irradiation.

were applied to examine the Cr valance state on the surface and in the bulk of the synthesized photocatalysts. XPS (Fig. 7a) reveals that the relative content of Cr^{6+} (580.2 eV) on the surface of the synthesized samples decreases in the order $SrTiO_3$(La,Cr) > Sr_2TiO_4(La,Cr) > $Sr_2TiO_4/SrTiO_3$(La,Cr), while the relative content of Cr^{3+} (576.5 eV) increases in the order $SrTiO_3$(La,Cr) < Sr_2TiO_4(La,Cr) < $Sr_2TiO_4/SrTiO_3$(La,Cr). This demonstrates that much fewer surface Cr^{6+} recombination sites are created on the surface of the $Sr_2TiO_4/SrTiO_3$(La,Cr) composite photocatalyst. Fig. 7b shows the EPR spectra of samples measured at 77 K. All of the samples show broad Cr^{3+} EPR signals with linewidth *ca.* 35 *G* and *g* value *ca.* 1.979.[35] The EPR intensity of Cr^{3+} in these samples is in the order $SrTiO_3$(La,Cr) ≈ Sr_2TiO_4(La,Cr) < $Sr_2TiO_4/SrTiO_3$(La,Cr). This further demonstrates that the $Sr_2TiO_4/SrTiO_3$(La,Cr) composite photocatalyst has a lower amount of Cr^{6+} formed not only on the surface, but also in the bulk. Note that these three samples were doped with the same amount of Cr under the same experimental conditions. Formation of a lower amount of Cr^{6+} throughout the $Sr_2TiO_4/SrTiO_3$(La,Cr) composite photocatalyst is beneficial for charge transfer and separation.

3.4 Time-resolved FT-IR spectroscopy

The time-resolved (ms) FT-IR (Fig. 8) was conducted to characterize the photogenerated electrons in the synthesized photocatalysts.[36] In micro-scale time-resolved FT-IR, the IR absorption intensity directly reflects the amount of long-lived electrons on the shallow traps, defects or those due to efficient charge separation.[37] It can be seen from Fig. 8 that the overall trends of the time decay profiles for the individual samples and the composite samples are quite similar except the IR intensity differences, indicating that these samples have different amounts of long-lived electrons (life-times in ms scale) which decay in similar ways. Because the photocatalytic activity of Sr_2TiO_4(La,Cr) is higher than that of $SrTiO_3$(La,Cr), the higher IR intensity of $SrTiO_3$(La,Cr) (Fig. 8a) than that of Sr_2TiO_4(La,Cr) (Fig. 8b) is an indication that the observed long-lived electrons in these two individual samples are mainly due to the electrons trapped by shallow traps/defect sites, such as Cr^{6+}. The possible assignment of the long-lived electrons due to electron traps on the Cr^{6+} defect sites is coincidentally in good agreement with the XPS and EPR results that Cr^{6+} content is higher in $SrTiO_3$(La,Cr) than in Sr_2TiO_4(La,Cr). It is also noted that the time resolved IR decay profile of $Sr_2TiO_4/SrTiO_3$(La,Cr) composite photocatalyst (Fig. 8c) lies between those of $SrTiO_3$(La,Cr) and Sr_2TiO_4(La,Cr). As shown in the previous sections, the $Sr_2TiO_4/SrTiO_3$(La,Cr) composite photocatalyst has a kind of superlattice macrostructure integrated with Sr_2TiO_4-(La,Cr) and $SrTiO_3$(La,Cr) nanoparticles (TEM) in an approximately 3 : 2 composition ratio (XRD). If there are no other effects on the $Sr_2TiO_4/SrTiO_3$(La,Cr) composite photocatalyst, it should show a time decay profile with 3/5 and 2/5 intrinsic characteristics of the individual Sr_2TiO_4(La,Cr) and $SrTiO_3$-(La,Cr), respectively. The time resolved IR decay profile of the simulated data based on this assumption has been plotted, as shown in Fig. 8d. It can be seen that the experimentally observed decay profile (Fig. 8c) shows higher IR intensity than that of the simulated decay profile (Fig. 8d), indicating that the composite $Sr_2TiO_4/SrTiO_3$(La,Cr) photocatalyst has much more long-lived electrons than expected. There might be some additional contributions to such long-lived electrons in the composite photocatalyst besides the shallow traps/defects. It is feasible to assign the additional long-lived electrons in the composite photocatalyst to the long-lived electrons generated by efficient charge transfer and separation across the heterojunctions.[38]

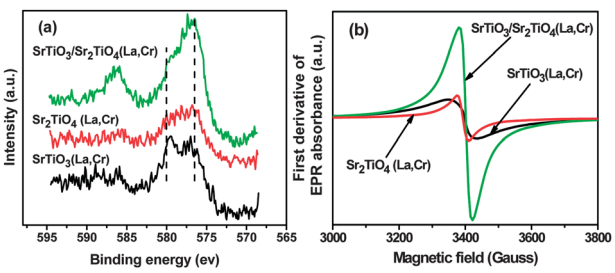

Fig. 7 (a) X-ray photoelectron spectra of Cr 2p, and (b) X-band EPR spectra of the samples.

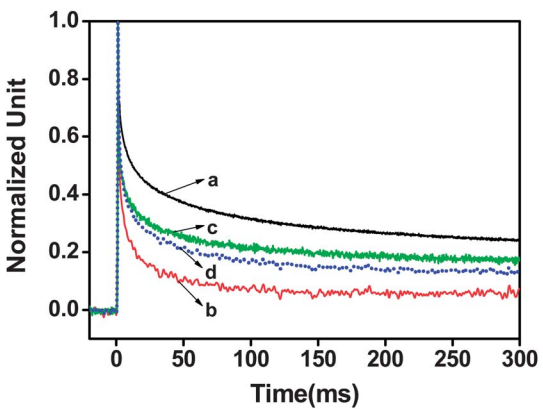

Fig. 8 Carrier relaxation dynamics of 0.3 wt% Pt loaded samples by normalized time-resolved FT-IR transient profiles of average IR absorption of (a) $SrTiO_3$(La,Cr), (b) Sr_2TiO_4(La,Cr), (c) $Sr_2TiO_4/SrTiO_3$(La,Cr), and (d) $Sr_2TiO_4/SrTiO_3$(La,Cr) (simulated based on the Sr_2TiO_4(La,Cr)/$SrTiO_3$(La,Cr) composition ratio of 3 : 2).

3.5 Mechanism of the photocatalytic reactions on the composite photocatalyst

Table 1 summarizes the bandgap energies and specific BET surface areas of the synthesized photocatalysts. It can be seen that the specific surface area of $SrTiO_3$(La,Cr) is 8.9 $m^2\ g^{-1}$, which is slightly larger than those of Sr_2TiO_4(La,Cr) and $Sr_2TiO_4/SrTiO_3$(La,Cr) (6.1 and 6.2 $m^2\ g^{-1}$, respectively). Since there is no big difference in surface area of these samples, the effect of the surface area on the high photocatalytic activity of the composite photocatalyst can be ruled out.

Based on the experimental results, the proposed model for enhanced H_2 production of $Sr_2TiO_4/SrTiO_3$(La,Cr) heterojunction is schematically illustrated in Scheme 1 (all of the potentials are normalized to NHE). When the photocatalyst was excited by visible light with photon energy higher or equal to the bandgaps of Sr_2TiO_4(La,Cr) and $SrTiO_3$(La,Cr), the electrons in the valance band could be excited to the conduction band, leaving the same amount of holes in the valance band. Since the conduction band edge potential of $SrTiO_3$(La,Cr) is more negative than that of Sr_2TiO_4(La,Cr), and the valance band edge potential of Sr_2TiO_4(La,Cr) is more positive than that of $SrTiO_3$(La,Cr), the photogenerated electrons and holes can readily transfer from $SrTiO_3$(La,Cr) to Sr_2TiO_4(La,Cr) and from Sr_2TiO_4(La,Cr) to $SrTiO_3$(La,Cr), respectively. As a result, the photogenerated electrons and holes can be more efficiently separated between the two components of the nanoparticles *via* the heterojunctions. Because the Pt nanoparticles were mainly deposited on the surface of Sr_2TiO_4(La,Cr), the separated electrons on Sr_2TiO_4(La,Cr) may further transfer to the Pt nanoparticles and participate in the surface reduction reaction for hydrogen evolution. The heterojunction structure, preferential deposition of Pt nanoparticles on the surface of Sr_2TiO_4(La,Cr) component, and the lower amount of Cr^{6+} electron trapping sites are the main reasons for the enhancement of the photocatalytic activity for the composite heterojunction photocatalyst.

4 Conclusion

In summary, we have prepared a composite $Sr_2TiO_4/SrTiO_3$-(La,Cr) heterojunction photocatalyst which shows higher photocatalytic activity compared to the individual $SrTiO_3$(La,Cr) and Sr_2TiO_4(La,Cr) for hydrogen production under visible light irradiation. The composite photocatalyst constitutes of a kind of superlattice macrostructure integrated with $SrTiO_3$(La,Cr) and Sr_2TiO_4(La,Cr) nanoparticles throughout the sample, and well defined heterojunctions are formed by matching the lattice fringes between $SrTiO_3$(La,Cr) and Sr_2TiO_4(La,Cr) components. Band structure analyses show that the photogenerated electrons and holes tend to migrate from $SrTiO_3$(La,Cr) to Sr_2TiO_4(La,Cr) and from Sr_2TiO_4(La,Cr) to $SrTiO_3$(La,Cr), respectively. The charge transfer and separation can be driven by the existing minor potential differences between the two components. Furthermore, codoping of La with Cr in $Sr_2TiO_4/SrTiO_3$(La,Cr) results in the presence of the doped Cr mainly in the form of Cr^{3+} rather than high valent Cr^{6+} species acting as electron trapping sites. Overall, the composite photocatalyst possesses a higher photocurrent in the photoelectrochemical measurements and more long-lived electrons due to efficient charge separation in the time resolved FT-IR spectroscopic study. Finally, the preferential loading of the Pt nanoparticles on the surface of the electron accepting component of Sr_2TiO_4(La,Cr) in the composite photocatalyst further facilitates the photocatalytic activity of the hydrogen evolution reaction. These results suggest that it is an effective method to improve the photocatalytic activity by the tailored design and synthesis of a composite photocatalyst possessing lattice and energy matching heterojunctions.

Acknowledgements

This work was financially supported by the National Natural Science Foundation of China under grant no. 21090341, 21061140361 and 20923001, National Basic Research Program (973 Program) of the Ministry of Science and Technology of China under grant no. 2009CB220010, and the Solar Energy Action Program of the Chinese Academy of Sciences under Grant no. KGCX2-YW-391. The authors thank Dr Gang Liu of Shenyang National Laboratory for Materials Science, Institute of Metal Research, Chinese Academy of Sciences, for XPS measurements, and Dr Dan Zhao in Solar Energy Division, Dalian National Laboratory for Clean Energy, for helping in determining the composition ratio of the composite photocatalyst by XRD data analysis.

Notes and references

1 X. Chen, S. Shen, L. Guo and S. S. Mao, *Chem. Rev.*, 2010, **110**, 6503.
2 H. Kato, K. Asakura and A. Kudo, *J. Am. Chem. Soc.*, 2003, **125**, 3082.
3 Y. Sakata, Y. Matsuda, T. Nakagawa, R. Yasunaga, H. Imamura and K. Teramura, *ChemSusChem*, 2011, **4**, 181.
4 T. Ohno, L. Bai, T. Hisatomi, K. Maeda and K. Domen, *J. Am. Chem. Soc.*, 2012, **134**, 8254.
5 L. Spanhel, H. Weller and A. Henglein, *J. Am. Chem. Soc.*, 1987, **109**, 6632.
6 W. T. Sun, Y. Yu, H. Y. Pan, X. F. Gao, Q. Chen and L. M. Peng, *J. Am. Chem. Soc.*, 2008, **130**, 1124.
7 Y. L. Lee, C. F. Chi and S. Y. Liau, *Chem. Mater.*, 2010, **22**, 922.
8 K. Domen, A. Kudo and T. Onishi, *J. Catal.*, 1986, **102**, 92.
9 X. B. Chen, Y. B. Lou, S. Dayal, X. F. Qiu, R. Krolicki, C. Burda, C. F. Zhao and J. Becker, *J. Nanosci. Nanotechnol.*, 2005, **5**, 1408.
10 G. Sheng, J. Li, S. Wang and X. Wang, *Progr. Chem.*, 2009, **21**, 2492.
11 G. Liu, L. Wang, H. G. Yang, H. M. Cheng and G. Q. Lu, *J. Mater. Chem.*, 2010, **20**, 831.
12 D. Wang, J. Ye, T. Kako and T. Kimura, *J. Phys. Chem. B*, 2006, **110**, 15824.
13 Z. G. Yi, H. Iwai and J. H. Ye, *Appl. Phys. Lett.*, 2010, **96**, 114103.
14 H. Kato and A. Kudo, *J. Phys. Chem. B*, 2002, **106**, 5029.

15 T. Ishii, H. Kato and A. Kudo, *J. Photochem. Photobiol., A*, 2004, **163**, 181.
16 S. Ouyang, H. Tong, N. Umezawa, J. Cao, P. Li, Y. Bi, Y. Zhang and J. Ye, *J. Am. Chem. Soc.*, 2012, **134**, 1974.
17 H. G. Kim, P. H. Borse, W. Y. Choi and J. S. Lee, *Angew. Chem., Int. Ed.*, 2005, **44**, 4585.
18 H. G. Kim, P. H. Borse, J. S. Jang, E. D. Jeong, O. S. Jung, Y. J. Suh and J. S. Lee, *Chem. Commun.*, 2009, 5889.
19 D. F. Wang, Z. G. Zou and J. H. Ye, *Chem. Mater.*, 2005, **17**, 3255.
20 J. Zhang, Q. Xu, Z. Feng, M. Li and C. Li, *Angew. Chem., Int. Ed.*, 2008, **47**, 1766.
21 X. Zong, H. Yan, G. Wu, G. Ma, F. Wen, L. Wang and C. Li, *J. Am. Chem. Soc.*, 2008, **130**, 7176.
22 X. Zong, G. Wu, H. Yan, G. Ma, J. Shi, F. Wen, L. Wang and C. Li, *J. Phys. Chem. C*, 2010, **114**, 1963.
23 B. Ma, J. Yang, H. Han, J. Wang, X. Zhang and C. Li, *J. Phys. Chem. C*, 2010, **114**, 12818.
24 M. Kakihana, *J. Sol-Gel Sci. Technol.*, 1996, **6**, 7.
25 G. Pfaff, *J. Mater. Chem.*, 1993, **3**, 721.
26 S. J. Tauster, S. C. Fung and R. L. Garten, *J. Am. Chem. Soc.*, 1978, **100**, 170.
27 H. Park and W. Choi, *J. Phys. Chem. B*, 2003, **107**, 3885.
28 J. Inaba and T. Katsufuji, *Phys. Rev. B: Condens. Matter Mater. Phys.*, 2005, **72**, 052408.
29 C. Sabathier, J. Chaumont, S. Rouziere and A. Traverse, *Nucl. Instrum. Methods Phys. Res., Sect. B*, 2005, **234**, 509.
30 N. Serpone, D. Lawless and R. Khairutdinov, *J. Phys. Chem.*, 1995, **99**, 16646.
31 O. Manasreh, *Semiconductor Heterojunctions and Nanostructures*, McGraw-Hill, New York, 2005.
32 S. N. Frank and A. J. Bard, *J. Am. Chem. Soc.*, 1975, **97**, 7427.
33 M. Paranthaman, A. Aruchamy, G. Aravamudan and G. V. S. Rao, *Mater. Chem. Phys.*, 1986, **14**, 349.
34 J. W. Shi, S. H. Shen, Y. B. Chen, L. J. Guo and S. S. Mao, *Opt. Express*, 2012, **20**, A351.
35 L. Zhu, M. Wang and J. Dang, *Appl. Magn. Reson.*, 2011, **41**, 45.
36 A. Yamakata, T. Ishibashi and H. Onishi, *J. Phys. Chem. B*, 2002, **106**, 9122.
37 T. Chen, Z. Feng, G. Wu, J. Shi, G. Ma, P. Ying and C. Li, *J. Phys. Chem. C*, 2007, **111**, 8005.
38 X. Wang, Q. Xu, M. Li, S. Shen, X. Wang, Y. Wang, Z. Feng, J. Shi, H. Han and C. Li, *Angew. Chem., Int. Ed.*, 2012, **51**, 13089.
39 A. Kudo and Y. Miseki, *Chem. Soc. Rev.*, 2009, **38**, 253.

